

# Absolute instabilities in a high-order-mode gyrotron traveling-wave amplifier

W. C. Tsai, T. H. Chang, N. C. Chen, and K. R. Chu

*Department of Physics, National Tsing Hua University, Hsinchu, Taiwan*

H. H. Song and N. C. Luhmann, Jr.

*Department of Applied Science, University of California, Davis, California 95616, USA*

(Received 24 March 2004; published 5 November 2004)

The absolute instability is a subject of considerable physics interest as well as a major source of self-oscillations in the gyrotron traveling-wave amplifier (gyro-TWT). We present a theoretical study of the absolute instabilities in a TE<sub>01</sub> mode, fundamental cyclotron harmonic gyro-TWT with distributed wall losses. In this high-order-mode circuit, absolute instabilities arise in a variety of ways, including overdrive of the operating mode, fundamental cyclotron harmonic interactions with lower-order modes, and second cyclotron harmonic interaction with a higher-order mode. The distributed losses, on the other hand, provide an effective means for their stabilization. The combined configuration thus allows a rich display of absolute instability behavior together with the demonstration of its control. We begin with a study of the field profiles of absolute instabilities, which exhibit a range of characteristics depending in large measure upon the sign and magnitude of the synchronous value of the propagation constant. These profiles in turn explain the sensitivity of oscillation thresholds to the beam and circuit parameters. A general recipe for oscillation stabilization has resulted from these studies and its significance to the current TE<sub>01</sub>-mode, 94-GHz gyro-TWT experiment at UC Davis is discussed.

DOI: 10.1103/PhysRevE.70.056402

PACS number(s): 84.40.Ik, 84.40.Fe

## I. INTRODUCTION

The gyrotron traveling-wave tube (gyro-TWT) is a millimeter-wave amplifier based on the electron cyclotron maser (ECM) instability. By employing a nonresonant fast-wave circuit, the gyro-TWT features high power and broad bandwidth, which makes it an attractive source for advanced radar and communication applications. In gyrodevices, the electrons resonantly interact with the electromagnetic wave under the synchronism condition,

$$\omega - k_z v_z - s\Omega_c \geq 0, \quad (1)$$

where  $\omega$  is the wave frequency,  $k_z$  is the propagation constant,  $v_z$  is the electron axial velocity,  $s$  is the cyclotron harmonic number, and  $\Omega_c$  is the relativistic electron cyclotron frequency. In a resonant cavity,  $\omega$  and  $k_z$  assume discrete values, which restricts cyclotron resonance to a narrow range of magnetic-field strength for each mode. In contrast, there are no such restrictions in the waveguide structure of the gyro-TWT. Consequently, the electrons can be in simultaneous resonance with a multitude of forward and backward waves both at the fundamental and higher cyclotron harmonics.

As an example, Fig. 1 plots the  $\omega$ - $k_z$  diagrams of the four lowest-order waveguide modes and the fundamental ( $s=1$ ) and second ( $s=2$ ) cyclotron harmonic beam-wave synchronism lines for a TE<sub>01</sub> mode, 94-GHz gyro-TWT operating at the fundamental cyclotron harmonic (parameters given in the figure caption). Instabilities occur at the intersections of the mode and synchronism lines, four of which are denoted by the mode indices (subscript) and cyclotron harmonic number (superscript). As is well understood, intersections in the backward-wave region are potential absolute instabilities,

while those in the forward-wave region are normally, but not always, convective instabilities. The gyro-TWT is a complicated case because it exploits a convective instability near the cutoff frequency (e.g., the operating point in Fig. 1), which transitions into an absolute instability at sufficiently high beam current when the unstable spectrum extends into the backward-wave region. One or more of these absolute instabilities can easily be the dominant source of oscillations in the gyro-TWT. Theoretical investigations of absolute instabilities can be found in Refs. [1–4].

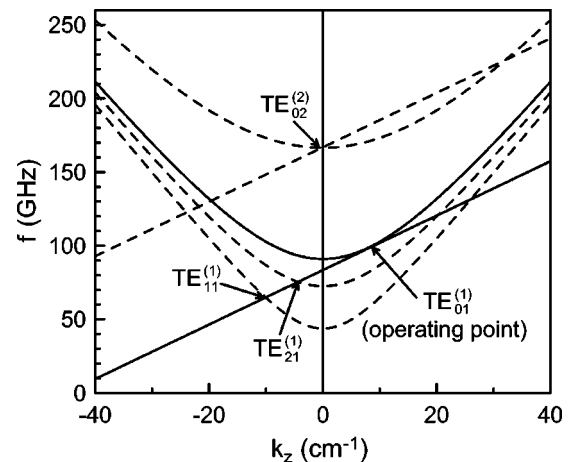


FIG. 1. Frequency vs  $k_z$  diagrams of the waveguide modes and the beam-wave synchronism lines for a TE<sub>01</sub>-mode, 94-GHz gyro-TWT operating at the fundamental cyclotron harmonic. Parameters used are (see also Table I): waveguide radius=0.201 cm, beam voltage=100 kV, velocity ratio ( $v_\perp/v_z$ )=1.0, and  $B_0=35.6$  kG. The applied magnetic field  $B_0$  is set at 0.995 of the grazing value ( $B_{g01}=35.8$  kG) for the operating mode.

There is an additional source of oscillation, which results from regenerative amplification due to end reflections. Such oscillations are common in traveling-wave structures. The reflective feedback loop can be effectively cut off by a sever or distributed losses (a long established practice in conventional linear-beam TWT's). The absolute instability, a much more serious problem to the gyro-TWT than to the conventional TWT, is basically different from the reflective oscillation in that the backward wave associated with the absolute instability is generated in an internal feedback loop.

The performance of early gyro-TWT experiments was severely limited by such oscillation problems [5,6]. Improved stability was subsequently demonstrated at the Naval Research Laboratory [7] and Varian Associates [8–10] by employing a distributed-loss circuit. However, experimental results during this early period generally fell short of theoretical predictions. Causes of the performance degradation (principally oscillation interferences) have been discussed at length in Ref. [11]. The understanding of these oscillations and methods for their suppression thus constitutes the principal challenges of gyro-TWT research.

A new round of international research activities started in the late 1980s, all with emphasis on the fundamental issues of stability and strongly supported by theories. Following Ref. [12], herein we present an updated review of these efforts as an illustration of the variety of schemes devised for oscillation stabilization. At the National Tsing Hua University, mode competition in a smooth, unloaded gyro-TWT circuit has been characterized in experiment [13] and analyzed with particle simulations [14]. The severity of the absolute instability was evidenced by the fact that, even in the lowest ( $TE_{11}$ ) mode operation at the fundamental cyclotron harmonic interaction, a  $TE_{21}$  second cyclotron harmonic oscillation set in at a beam current as low as 0.1 A. A later attempt to suppress oscillations with a severed circuit was partially successful, increasing the oscillation threshold to 0.9 A [15]. More detailed modeling led to the demonstration of stable operation at 3 A beam current in a distributed-loss circuit coated with Aquadag® [4]. Then, taking advantage of the fact that the wall resistivity reduces the device gain at only one-third of the damping rate of the cold mode [16], an ultrahigh gain scheme has been demonstrated in a 35-GHz,  $TE_{11}$ -mode gyro-TWT, producing 93 kW saturated output power at 70 dB stable gain and 26.5% efficiency with a 3-dB bandwidth of 8.6% [17,18]. A waveguide coated with Aquadag® is incompatible with high average-power operation, although invaluable for such physics studies. For increased tolerance to wall heating, the NRL group has recently built a 35-GHz,  $TE_{01}$ -mode gyro-TWT employing ceramic rings for distributed attenuation. The experiment produced 137 kW saturated power at 47 dB gain and 17% efficiency in zero-drive stable operation, with a corresponding 3-dB bandwidth of 3.3% [19].

In another approach, slotted and axially sliced waveguides have been employed by the UCLA and UC Davis group to suppress unwanted azimuthal modes. Saturated third harmonic operation was demonstrated in a slotted structure, achieving 3% bandwidth and 6 kW output power with 5% efficiency and 11 dB gain at the center frequency of 10 GHz [20]. In a separate experiment, stability was achieved for the

$TE_{21}$  mode with an axially sliced waveguide designed to suppress the odd-order azimuthal modes. This second harmonic experiment produced the highest gyro-TWT output power to date (207 kW at 16.7 GHz) for a moderately energetic electron beam [21,22]. The current research focus of the group is on a  $TE_{01}$ -mode, 94-GHz gyro-TWT with a distributed-loss circuit [23].

Two-stage circuits can increase the stability threshold as well as provide other advantages. The NRL group developed a sophisticated circuit comprised of two tapered rectangular interaction sections isolated by a short cutoff section. The input signal was preamplified in the first stage. The wave was then reflected at the cutoff section, while the imbedded signal in the electron beam was amplified again in the second stage. This two-stage approach allowed broadband (20%, centered at 35 GHz) operation at 8 kW saturated output power, 25 dB gain, and 16% efficiency [24]. The University of Maryland group has been conducting research on two-stage frequency-multiplying schemes, including a frequency-doubling inverted gyro-twystron [25,26] and a frequency-doubling gyro-TWT [27]. Traveling-wave amplification forms the first stage in the former scheme, and both stages in the latter. Operation of the inverted gyro-twystron [25] and its phase characteristics [26] were recently reported.

Recently, a Russian and United Kingdom team developed a helically corrugated interaction structure [28]. The corrugation alters the low- $k_z$  portion of the waveguide dispersion curve to an approximate straight line centered at the  $k_z=0$  point. This novel circuit provides the important advantages of stability, broad bandwidth, and relative insensitivity to the electron velocity spread. For the hot test, a 185-keV linear electron beam was passed through a magnetic kicker to acquire the required perpendicular velocity. A second harmonic experiment produced 1.1 MW output power at 37 dB gain, 29% efficiency, and 21% bandwidth [29,30].

More recently, the MIT group built a 140-GHz gyro-TWT employing a confocal waveguide for high-order-mode operation. This quasioptical circuit promises high-average-power operation deep in the millimeter-wave regime. The initial test has demonstrated 30-kW peak power in the  $HE_{06}$  mode with a gain of 29 dB and an unsaturated bandwidth of 2.3 GHz[31].

The current study addresses absolute instabilities in a gyro-TWT with distributed wall losses. The simplest case, fundamental harmonic operation in a  $TE_{11}$ -mode circuit, has been studied in considerable detail [4,17,18]. It was shown that the dominant source of oscillation arises from a second cyclotron harmonic,  $TE_{21}$  absolute instability. Our focus here will be a  $TE_{01}$ -mode, 94-GHz gyro-TWT recently designed [23] and currently in operation at UC Davis [32]. In this higher-order-mode circuit, oscillations cover a full range of possibilities. In addition to the absolute instability on the operating mode, neighboring modes of both higher and lower orders can also be absolutely unstable. Following a discussion of the theory background (Sec. II), we illustrate the different physical processes involved and the resultant field structures through the UC Davis gyro-TWT (Sec. III). The physical insights thus gained constitute the basis for an extensive examination of the parametric sensitivity of the most

likely absolute instabilities (Sec. IV), which leads to a general recipe for achieving zero-drive stability (Sec. V).

## II. CONVECTIVE AND ABSOLUTE INSTABILITIES—A BRIEF SUMMARY

Assuming a uniform system of infinite length, the ECM instability in the gyro-TWT is characterized by a dispersion relation,

$$D(\omega, k_z) = 0, \quad (2)$$

which determines how an initial disturbance will grow in the linear stage. Instabilities are generally classified into two types: convective and absolute. Operation of the gyro-TWT is based on a convective instability. The input wave is amplified while propagating forward with the beam. Thus in steady state the wave amplitude increases along the axis, but maintains a constant value at any fixed point in space. The operation is zero-drive stable in the sense that there is no output power without an input signal.

The dispersion relation of the gyro-TWT governs the linear (i.e., small signal) gain over a finite bandwidth. At a sufficiently high beam current, however, the gain spectrum can extend into the negative  $k_z$  region. Furthermore, synchronous interaction of the electron beam with other waveguide modes, at the fundamental or higher cyclotron harmonics, can readily take place in the negative  $k_z$  region (Fig. 1). A noise-level disturbance will then be amplified in the backward direction, thereby providing feedback to bunch incoming electrons. The disturbance can thus grow locally and spread out in both directions to result in self-oscillations. An instability of this type, characterized by growth at every spatial point, is referred to as the absolute instability.

The plasma physics criteria regarding the classification of absolute and convective instabilities can be found in Sturrock [33], Briggs [34], and Stix [35]. Taking Eq. (2) as an example and assuming the  $\exp(-i\omega t + ik_z z)$  dependence for the rf fields, the criteria state that there exists an instability of either the convective or absolute type if, for some real value of  $k_z$ , Eq. (2) has a solution for  $\omega$  with a positive imaginary part. The instability is absolute if both of the following two conditions are met. Otherwise, it is a convective instability.

*Condition 1.* For some  $\omega$  (let it be  $\omega_s$ ) with a positive imaginary part, Eq. (2) has a double root for  $k_z$  (let it be  $k_{zs}$ ). Algebraically, this condition implies that, in the upper half of the complex  $\omega$  plane, there exists a solution  $(\omega_s, k_{zs})$  of both Eq. (2) and its derivative,

$$\frac{\partial D(\omega, k_z)}{\partial k_z} = 0. \quad (3)$$

*Condition 2.* Along the path of  $\omega = \omega_s + i\sigma$  with  $\sigma$  increasing from zero to positive infinity, the double root  $k_{zs}$  of Eq. (2) splits into two separate roots. One root has the same sign for its imaginary part as that of  $k_{zs}$ , while the imaginary part of the other root experiences a sign change.

On the basis of these two conditions, analytical expressions for the threshold of the absolute instability have been derived in Refs. [1,3]. A graphical method for absolute instability identification can be found in Ref. [2].

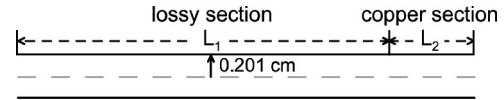


FIG. 2. Configuration of the  $TE_{01}$ -mode, 94 GHz gyro-TWT interaction circuit.

As a further point of interest, the asymptotic expressions for the rf fields vary in time and space as [34]

$$E, B \propto \frac{\exp(-i\omega_s t + ik_{zs} z)}{\sqrt{t}}. \quad (4)$$

Thus the real and imaginary parts of  $\omega_s$  give, respectively, the oscillation frequency and local growth rate of the absolute instability. The real part of  $k_{zs}$  gives the wavelength, while the imaginary part of  $k_{zs}$  imposes a spatial envelope on the field profile. Different envelope structures will be illustrated in the following section.

## III. CHARACTERIZATION OF ABSOLUTE INSTABILITIES IN THE GYRO-TWT

To illustrate the diverse behavior of the absolute instability, we begin with a stability analysis of the UC Davis gyro-TWT. The interaction circuit (Fig. 2) consists of a lossy section followed by a copper section. Both sections are assumed to have the same radius. Specific circuit and beam parameters together with the predicted performance are listed in Table I [23]. The amplification is based on the  $TE_{01}$  convective instability near the fundamental cyclotron harmonic frequency (the operating point in Fig. 1). However, numerous possibilities of oscillations exist as discussed in Sec. I. The lossy section is effective in stabilizing both the reflective and absolute instabilities [17,18]. Similar to the sever, the lossy section cuts off the path of the reflective feedback loop. In contrast to the sever, however, it is an integral part of the linear amplification stage. To the predominantly backward power flow of the absolute instability, the lossy section also functions as an effective energy sink.

We employ a single-mode, particle-tracing code as the principal tool for numerical calculations. Space charge effects are neglected and the applied magnetic field is assumed to be uniform throughout the interaction region. The transverse mode profile is approximated by that of a uniform waveguide. Outgoing-wave boundary conditions are imposed at both ends. With the electron beam treated as an ac current source, the oscillation frequency and axial field profile can then be self-consistently evaluated from the set of wave and electron dynamical equations. A detailed formalism can be found in Ref. [18]. We note in particular that the circuit loss is modeled here as a perturbation to the eigenmode of an unloaded cylindrical waveguide. This is a valid approximation for the use of a thin lossy layer on the waveguide walls, as in the UC Davis gyro-TWT circuit. However, as discussed by Calame *et al.* [36], in the case where the loss is achieved by lossy ceramics with finite thickness, the correct circuit losses would have to be calculated by full eigenmode solutions of a dielectric loaded cylindrical waveguide.

TABLE I. Design parameters of the UC Davis gyro-TWT amplifier.

Operating mode	$TE_{01}$
Cyclotron harmonic	fundamental
Waveguide radius ( $r_w$ )	0.201 cm
Cutoff frequency	91.0 GHz
Lossy section length ( $L_1$ )	11.7 cm
Wall resistivity ( $\rho$ )	$70\ 000\rho_{cu}$
Copper section length ( $L_2$ )	2.64 cm
Total circuit length ( $L_1+L_2$ )	14.34 cm
Beam voltage ( $V_b$ )	100 kV
Beam current ( $I_b$ )	5 A
Velocity ratio ( $v_\perp/v_z$ )	1.0
Velocity spread ( $\Delta v_z/v_z$ )	5%
Guiding center position ( $r_c$ )	$0.45r_w$
Applied magnetic field ( $B_0$ )	35.6 kG
Grazing magnetic field ( $B_{g01}$ )	35.8 kG
$B_0/B_{g01}$	0.995
Saturated output power	140 kW
Saturated efficiency	28%
Saturated gain	50 dB
Saturated bandwidth	5%

In an interaction circuit with distributed losses, axial mode structures are rather complicated and the lowest-order axial mode is not necessarily the mode with the lowest start-oscillation current ( $I_{st}$ ). For simplicity, we shall only be concerned with the axial mode with the lowest  $I_{st}$ . Calculations indicate that absolute instabilities associated with the  $TE_{02}$  ( $s=2$ ),  $TE_{21}$  ( $s=1$ ), and  $TE_{11}$  ( $s=1$ ) modes constitute the most serious concern because of their relatively low oscillation thresholds. In addition, the operating  $TE_{01}$  ( $s=1$ ) mode may become an absolute instability in an above-grazing magnetic field or at a large beam current. Hence these four modes (Fig. 1) will be the focus of subsequent studies.

Figure 3 shows how the start-oscillation current is deduced from the calculated oscillation powers of the four modes as functions of the beam current. Other parameters are given in Table I. For each mode, the oscillation starts at the beam current at which the efficiency approaches zero. It can be seen that, at the design current of 5 A, the operating  $TE_{01}$  mode is stable and the  $TE_{11}$  mode is marginally unstable, whereas both the  $TE_{02}$  and  $TE_{21}$  modes are expected to self-oscillate.

Figure 4 displays the field profiles of the four modes in Fig. 3 at their respective  $I_{st}$ . Two features are noticeable in this figure. First, there is a clear distinction between high- $k_z$  and low- $k_z$  modes. Wall losses are less effective in damping the high- $k_z$  modes than the low- $k_z$  modes [37]. Thus the greater the  $k_z$  magnitude, the further the field penetrates into the lossy region. In addition, for the same  $k_z$  value, wall losses are less effective in damping a low-order TE mode more than it damps a high-order TE mode [37]. For the present case, the  $TE_{11}$  mode is not only the lowest order mode, but also propagates with the largest  $k_z$  (Fig. 1). Hence

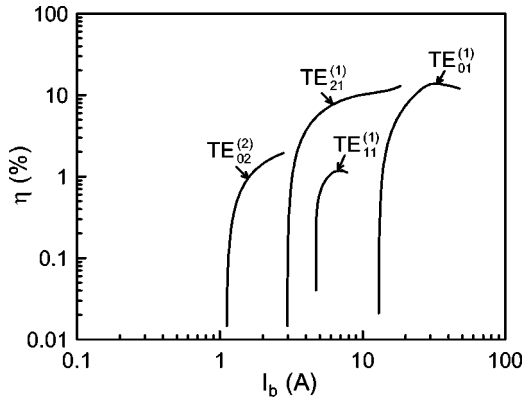


FIG. 3. Interaction efficiencies of the four most likely oscillating modes as functions of the beam current. For each mode, the oscillation starts at the beam current at which the efficiency approaches zero.

its field penetrates deepest into the lossy section.

As a second feature of Fig. 4, we observe the three possible field envelopes of the absolute instability predicted by Eq. (4) and determined by the imaginary part of  $k_{zs}$ . The positive- $k_z$  mode [ $TE_{01}$ , Fig. 4(a)] has a field pattern dominated by a forward-wave component. The low- $k_z$  mode [ $TE_{02}$ , Fig. 4(b)] has comparable forward and backward components and consequently forms a full standing-wave pattern. By contrast, the field profiles of the negative- $k_z$  modes [ $TE_{21}$  and  $TE_{11}$ , Figs. 4(c) and 4(d), respectively]

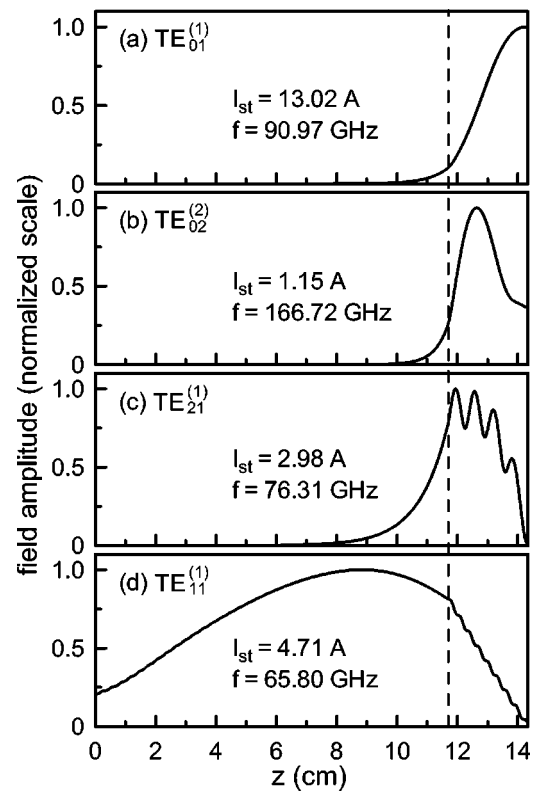


FIG. 4. Field profiles of the four modes in Fig. 3 at their respective start-oscillation current. Interface between the lossy and copper sections is indicated by the dashed line.

TABLE II. Reference parameters for studies of the parametric sensitivity of the start-oscillation current.

Waveguide radius ( $r_w$ )	0.201 cm
Lossy section length ( $L_1$ )	11.7 cm
Wall resistivity ( $\rho$ )	$70\,000\rho_{cu}$
Copper section length ( $L_2$ )	2.64 cm
Beam voltage ( $V_b$ )	100 kV
Velocity ratio ( $v_\perp/v_z$ )	1.0
Velocity spread ( $\Delta v_z/v_z$ )	5%
Guiding center position ( $r_c$ )	$0.45r_w$
$B_0/B_{g01}$	0.995

consist of essentially backward waves. Some reflection takes place at the interface between the lossy and copper sections, which results in the field ripples of the negative- $k_z$  modes.

#### IV. PARAMETRIC DEPENDENCE OF THE OSCILLATION THRESHOLD

A subset of parameters taken from Table I is listed in Table II as a reference point in the vast parameter space. To isolate the effect of a particular parameter on the oscillation threshold, start-oscillation currents of the four most likely oscillations are calculated by varying only one parameter at a time. With the exception of the wall radius ( $r_w$ ) and guiding center position ( $r_c$ ), all of the reference parameters in Table II will be thus varied. We note again that the operating ( $TE_{01}$ ) mode exploits a convective instability near the cutoff frequency (Fig. 1), which transitions into an absolute instability at sufficiently high beam current when the unstable spectrum extends into the backward-wave region. The start-oscillation current for this mode refers to the minimum current required for such feedback-induced self-oscillations. At currents below the start-oscillation value, the system is still convectively unstable in the sense that a drive wave can be amplified in its passage through the interaction structure.

We first consider the more obvious parametric dependences of  $I_{st}$ . Figure 5 displays  $I_{st}$  of these four modes as a function of the velocity ratio  $\alpha (=v_\perp/v_z)$ . The beam-wave interaction is stronger at higher  $\alpha$  values. This results in the monotonic decrease of  $I_{st}$  as  $\alpha$  increases. Figure 6 displays  $I_{st}$  of the same modes as a function of the beam axial velocity spread  $\Delta v_z$  (standard deviation from the mean value  $v_{z0}$ ) normalized to  $v_{z0}$ . The velocity spread weakens the interaction and hence leads to an increase in  $I_{st}$ . As seen in the synchronism condition [Eq. (1)], the effect of a spread in  $v_z$  is magnified by the propagation constant  $k_z$ . Thus of the four modes considered,  $I_{st}$  of the  $TE_{11}$  mode shows the greatest sensitivity to  $\Delta v_z$  because the  $TE_{11}$  mode is excited at the largest  $k_z$  value (Fig. 1).

Figure 7(a) plots  $I_{st}$  for each of the four modes as a function of the parameter  $B_0/B_g$ , where  $B_g$  is the grazing magnetic field of the respective mode. For all the modes,  $I_{st}$  rises sharply to infinity as  $B_0/B_g$  falls below unity and hence out of the range of beam-wave synchronism. However, the gen-

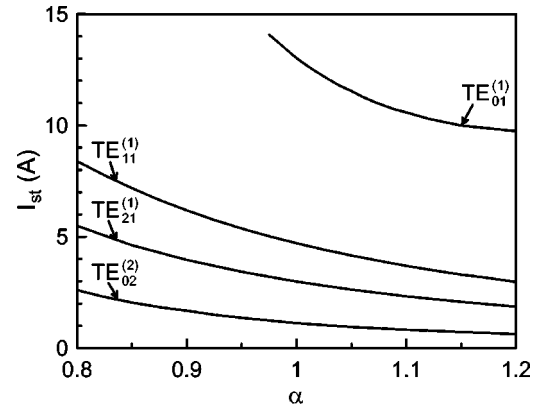


FIG. 5. Start-oscillation currents versus the velocity ratio  $\alpha$ , all showing monotonically decreasing values with increased  $\alpha$ .

eral behavior of  $I_{st}$  as a function of  $B_0/B_g$  can be classified in accordance with the physical processes involved. The azimuthal bunching forces responsible for the ECM instability are partially offset by the axial debunching forces with a magnitude proportional to  $k_z$  [38,39]. Thus  $I_{st}$  of the  $TE_{01}$ ,  $TE_{02}$ , and  $TE_{21}$  modes reaches a minimum when the synchronism line intersects with the mode line at a point near the cutoff frequency ( $k_z \approx 0$  or  $B_0/B_g \approx 1.08$ ), where the axial debunching forces are vanishingly small. However, unlike the  $TE_{01}$ ,  $TE_{02}$ , and  $TE_{21}$  modes whose fields reside essentially in the copper section, the  $TE_{11}$  mode penetrates deeper into the lossy section (the reasons were discussed in Sec. III). The additional interaction length prolongs the beam-wave interaction, whereas the larger  $k_z$  weakens the interaction strength because of stronger axial debunching forces and increased susceptibility to beam velocity spread. As a result of the opposing trends of these processes,  $I_{st}$  of the  $TE_{11}$  mode minimizes at a nonzero  $k_z$  (at  $B_0/B_g \approx 1.45$ ) beyond which the weakening effects of axial debunching and velocity spread start to outweigh the benefit of field penetration.

Because the normalization factor  $B_g$  differs from mode to mode, each curve in Fig. 7(a) is plotted on a different absolute scale of  $B_0$ . Figure 7(b) displays  $I_{st}$  on the same  $B_0$  scale over a much narrower range around  $B_0/B_{g01}=1$ . This is the

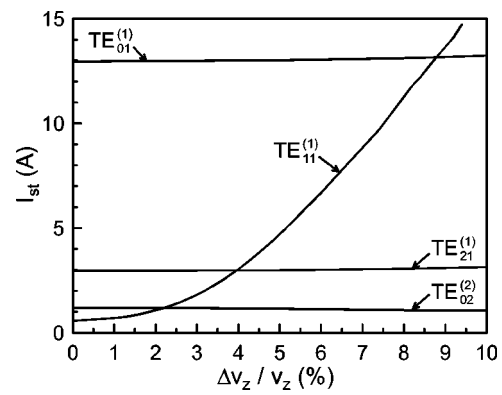


FIG. 6. Start-oscillation currents versus the beam axial velocity spread. Modes excited at larger  $k_z$  values exhibit greater sensitivity to the velocity spread.

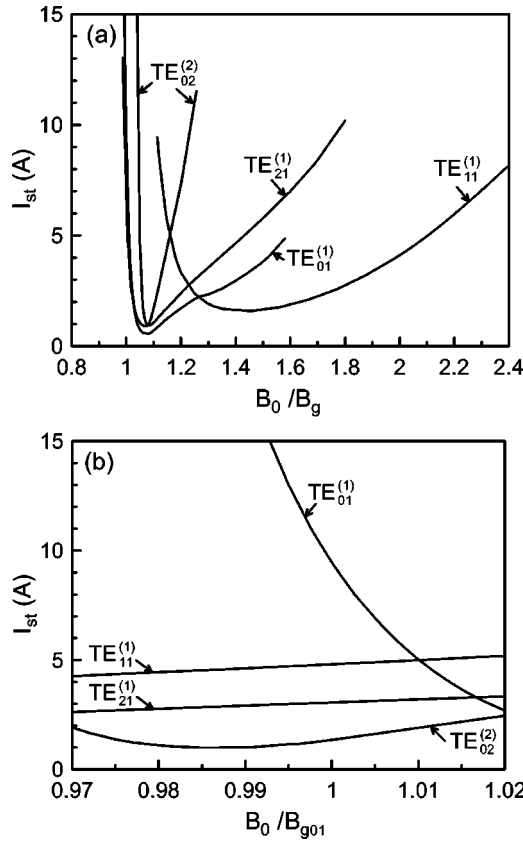


FIG. 7. (a) Start-oscillation currents versus  $B_0/B_g$ , where  $B_g$  is the grazing magnetic of the respective mode. In this figure, different modes are displayed on different absolute magnetic field scales. (b) Start-oscillation currents plotted on the same absolute magnetic field scale over a narrow range around the grazing magnetic field of the operating mode  $B_{g01}$ .

operating range of the UC Davis gyro-TWT. The results are consistent with the  $I_{st}$  shown in Fig. 3. The operating  $TE_{01}$  mode is seen to be stable against self-oscillations at the design value of  $B_0/B_{g01}=0.995$ . However, the other modes must be stabilized by means other than magnetic field tuning.

Figure 8 plots  $I_{st}$  of the four modes as functions of the beam voltage ( $V_b$ ). The slope of the synchronism line is proportional to  $v_z$  (Fig. 1). Thus as the voltage increases while

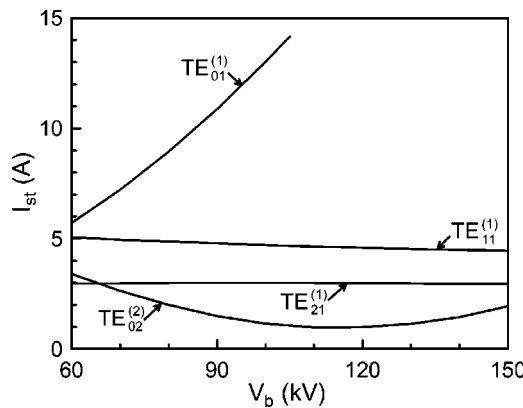


FIG. 8. Start-oscillation currents versus the beam voltage  $V_b$ .

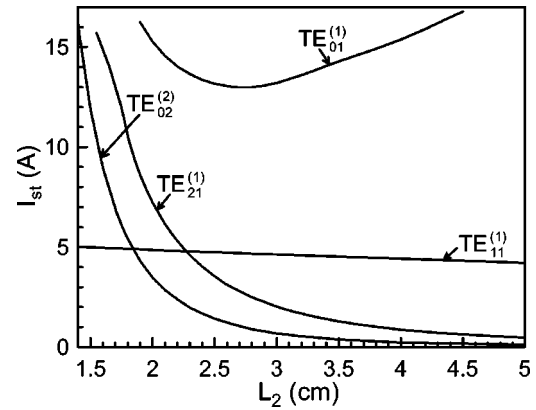


FIG. 9. Start-oscillation currents versus the copper section length  $L_2$ .

maintaining the same  $\alpha$  value, the synchronism line steepens and the near-grazing intersection point with the  $TE_{01}$  mode shifts away from the backward-wave region. This results in a higher  $I_{st}$  for the operating mode. On the other hand, the oscillation has the minimum  $I_{st}$  at  $V_b \approx 110$  kV, for which the synchronism line for the second cyclotron harmonic intercepts the  $TE_{02}$  mode line at the smallest  $k_z$  value.

Figure 9 plots  $I_{st}$  of the four modes as functions of the copper section length ( $L_2$ ). The start-oscillation current of the  $TE_{11}$  mode depends weakly on  $L_2$  because the  $TE_{11}$  field resides principally in the much longer lossy section (Fig. 4). By comparison, fields of the other three modes are mostly confined inside the copper section. Thus poor bunching in the short copper section results in increased  $I_{st}$ . For the  $TE_{01}$  mode, however,  $I_{st}$  increases again when  $L_2 > 2.7$  cm, where the oscillation frequency approaches the cutoff value and consequently the field is strongly damped by wall losses.

Deeper penetration of the fields into the lossy section also explains the greater sensitivity of the  $TE_{11}$  oscillation threshold to the lossy section length ( $L_1$ ) as shown in Fig. 10. For the same reason, Fig. 11 indicates that  $I_{st}$  of the  $TE_{11}$  oscillation is more sensitive to the wall resistivity than the other three modes.

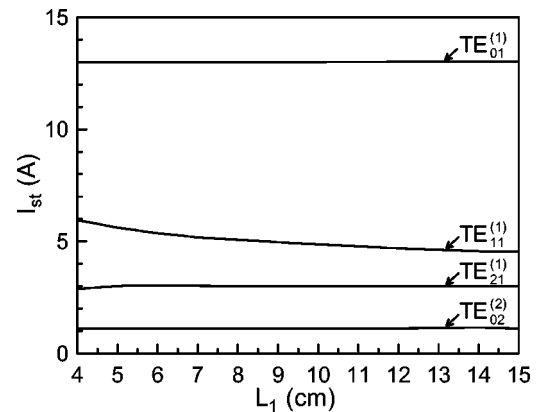


FIG. 10. Start-oscillation currents versus the lossy section length  $L_1$ .

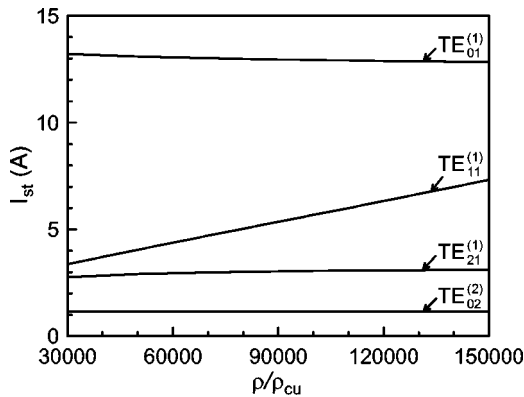


FIG. 11. Start-oscillation currents versus the wall resistivity  $\rho$  of the lossy section ( $\rho$  is normalized to the resistivity of copper  $\rho_{cu}$ ).

## V. SUMMARY AND CONCLUSION

We have examined the diversity of the absolute instability behavior and the physical processes involved through the example of a  $TE_{01}$ -mode, 94-GHz gyro-TWT with distributed wall losses. The high-order-mode circuit brings into play a variety of oscillating modes characterized by the sign and magnitude of the synchronous propagation constant  $k_z$ . These oscillations can exhibit a spatial envelope leaning either forward or backward depending upon the sign of  $k_z$  [Figs. 4(a), 4(c), and 4(d)], or assume the form of a standing wave in the case of a vanishingly small  $k_z$  [Fig. 4(b)]. As a consequence of the competing processes among the field penetration, debunching forces, and the velocity-spread degradation, different oscillations thrive under different conditions. Fields of high- $k_z$  and low-order modes penetrate deeper into the lossy section [Fig. 4(d)] thereby resulting in a longer interaction length. On the other hand, the interaction

strength of high- $k_z$  modes is reduced by the axial debunching forces and increased sensitivity to the beam velocity spread (Fig. 6). The opposite is true for the low- $k_z$  and high-order modes, which are more strongly damped by wall losses and hence more readily confined to the copper output section [Figs. 4(a)–4(c)]. However, they are also less sensitive to the beam velocity spread (Fig. 6).

Clarification of the oscillation behavior and its interplay with wall losses suggests different remedies for different types of oscillations. As a general recipe for achieving zero-drive stability, one first suppresses the growth of high- $k_z$  and low-order modes in a lossy section with sufficient wall losses. The reduction in amplifier gain is only one-third of the cold tube attenuation [16] and can thus be compensated for by a lengthened lossy section [17,18]. With their fields confined to the copper section, the remaining oscillating modes can then be effectively stabilized by a reduction of the copper section length. This will be at the expense of slightly reduced interaction efficiency for the operating mode. As a specific example, the UC Davis gyro-TWT is predicted to be stable against the  $TE_{01}$  absolute instability, but susceptible to  $TE_{11}$ ,  $TE_{21}$ , and  $TE_{02}$  oscillations (Fig. 3). In light of current studies, complete stabilization can be achieved with a 20% increase in wall losses to stabilize the  $TE_{11}$  oscillation (Fig. 11) and a 30–35% reduction of the copper section length to stabilize the  $TE_{21}$  and  $TE_{02}$  oscillations (Fig. 9).

## ACKNOWLEDGMENTS

This work is sponsored by the National Science Council, Taiwan, and AFOSR under Grant Nos. F49620-99-1-0297 (MURI MVE) and F49620-00-1-0339. The authors are grateful to K.F. Pao, Dr. D.B. McDermott, and Dr. L.R. Barnett for helpful discussions.

- 
- [1] Y. Y. Lau, K. R. Chu, L. R. Barnett, and V. L. Granatstein, Int. J. Infrared Millim. Waves **2**, 373 (1981).
  - [2] K. R. Chu and A. T. Lin, IEEE Trans. Plasma Sci. **16**, 90 (1988).
  - [3] J. A. Davies, Phys. Fluids B **1**, 663 (1989).
  - [4] K. R. Chu, L. R. Barnett, H. Y. Chen, S. H. Chen, Ch. Wang, Y. S. Yeh, Y. C. Tsai, T. T. Yang, and T. Y. Dawn, Phys. Rev. Lett. **74**, 1103 (1995).
  - [5] J. L. Seftor, V. L. Granatstein, K. R. Chu, P. Sprangle, and M. E. Read, IEEE J. Quantum Electron. **15**, 848 (1979).
  - [6] L. R. Barnett, K. R. Chu, J. M. Baird, V. L. Granatstein, and A. T. Drobot, in *Technical Digest of the International Electron Devices Meeting* (IEEE, New York, 1979) p. 164.
  - [7] L. R. Barnett, J. M. Baird, Y. Y. Lau, K. R. Chu, and V. L. Granatstein, in *Technical Digest of the International Electron Devices Meeting* (IEEE, New York, 1980) p. 314.
  - [8] R. S. Symons, H. R. Jory, and S. J. Hegji, in *Technical Digest of the International Electron Devices Meeting* (IEEE, New York, 1979) p. 676.
  - [9] P. E. Ferguson and R. S. Symons, in *Technical Digest of the International Electron Devices Meeting* (IEEE, New York,
  - 1980) p. 310.
  - [10] R. S. Symons, H. R. Jory, S. J. Hegji, and P. E. Ferguson, IEEE Trans. Microwave Theory Tech. **29**, 181 (1981).
  - [11] R. S. Symons and H. R. Jory, in *Advances in Electronics and Electron Physics*, edited by L. Marton and C. Marton (Academic, New York, 1981) Vol. 55, p. 1.
  - [12] K. R. Chu, IEEE Trans. Plasma Sci. **30**, 903 (2002).
  - [13] L. R. Barnett, L. H. Chang, H. Y. Chen, K. R. Chu, Y. K. Lau, and C. C. Tu, Phys. Rev. Lett. **63**, 1062 (1989).
  - [14] K. R. Chu, L. R. Barnett, W. K. Lau, L. H. Chang, A. T. Lin, and C. C. Lin, Phys. Fluids B **3**, 2403 (1991).
  - [15] K. R. Chu, L. R. Barnett, W. K. Lau, L. H. Chang, and C. S. Kou, in *Technical Digest of International Electron Devices Meeting* (IEEE, New York, 1990) p. 699.
  - [16] Y. Y. Lau, K. R. Chu, L. R. Barnett, and V. L. Granatstein, Int. J. Infrared Millim. Waves **2**, 395 (1981).
  - [17] K. R. Chu, H. Y. Chen, C. L. Hung, T. H. Chang, L. R. Barnett, S. H. Chen, and T. T. Yang, Phys. Rev. Lett. **81**, 4760 (1998).
  - [18] K. R. Chu, H. Y. Chen, C. L. Hung, T. H. Chang, L. R. Barnett, S. H. Chen, T. T. Yang, and D. Dialetis, IEEE Trans. Plasma Sci. **27**, 391 (1999).

- [19] M. Garven, J. P. Calame, B. G. Danly, K. T. Nguyen, B. Levush, F. N. Wood, and D. E. Pershing, IEEE Trans. Plasma Sci. **30**, 885 (2002).
- [20] C. K. Chong, D. B. McDermott, and N. C. Luhmann, Jr., IEEE Trans. Plasma Sci. **26**, 500 (1998).
- [21] Q. S. Wang, D. B. McDermott, and N. C. Luhmann, Jr., Phys. Rev. Lett. **75**, 4322 (1995).
- [22] Q. S. Wang, D. B. McDermott, and N. C. Luhmann, Jr., IEEE Trans. Plasma Sci. **24**, 700 (1996).
- [23] D. B. McDermott, H. H. Song, Y. Hirata, A. T. Lin, T. H. Chang, H. L. Hsu, P. S. Marandos, J. S. Lee, K. R. Chu, and N. C. Luhmann, Jr., IEEE Trans. Plasma Sci. **30**, 894 (2002).
- [24] G. S. Park, J. J. Choi, S. Y. Park, C. M. Armstrong, A. K. Ganguly, R. H. Kyser, and R. K. Parker, Phys. Rev. Lett. **74**, 2399 (1995).
- [25] H. Guo, S. H. Chen, V. L. Granatstein, J. Rogers, G. S. Nusinovich, M. Waters, B. Levush, and W. J. Chen, Phys. Rev. Lett. **79**, 515 (1997).
- [26] J. Rodgers, H. Guo, G. S. Nusinovich, and V. L. Granatstein, IEEE Trans. Electron Devices **48**, 2434 (2001).
- [27] K. R. Chu, H. Guo, and V. L. Granatstein, Phys. Rev. Lett. **78**, 4661 (1997).
- [28] G. G. Denisov, V. L. Bratman, A. D. R. Phelps, and S. V. Samsonov, IEEE Trans. Plasma Sci. **26**, 508 (1998).
- [29] G. G. Denisov, V. L. Bratman, A. W. Gross, W. He, A. D. R. Phelps, K. Ronald, S. V. Samsonov, and C. G. Whyte, Phys. Rev. Lett. **81**, 5680 (1998).
- [30] V. L. Bratman, A. W. Gross, G. G. Denisov, W. He, A. D. R. Phelps, K. Ronald, S. V. Samsonov, C. G. Whyte, and A. R. Young, Phys. Rev. Lett. **84**, 2746 (2000).
- [31] J. R. Sirigiri, M. A. Shapiro, and R. J. Temkin, Phys. Rev. Lett. **90**, 258302 (2003).
- [32] H. H. Song, D. B. McDermott, Y. Hirata, L. R. Barnett, C. W. Domier, H. L. Hsu, T. H. Chang, W. C. Tsai, K. R. Chu, and N. C. Luhmann, Jr., Phys. Plasmas **11**, 2935 (2004).
- [33] P. A. Sturrock, Phys. Rev. **112**, 1488 (1958).
- [34] R. J. Briggs, *Electron-Stream Interaction with Plasmas* (MIT, Cambridge, MA, 1964).
- [35] T. W. Stix, *Waves in Plasmas* (AIP, New York, 1992).
- [36] J. P. Calame, M. Garven, B. G. Danly, B. Levush, and K. T. Nguyen, IEEE Trans. Electron Devices **49**, 1469 (2002).
- [37] R. E. Collin, *Foundations for Microwave Engineering*, 2nd ed. (McGraw-Hill, New York, 1992), p. 197.
- [38] K. R. Chu and J. L. Hirshfield, Phys. Fluids **21**, 461 (1978).
- [39] K. R. Chu, Rev. Mod. Phys. **76**, 489 (2004).